iScience

CellPress
OPEN ACCESS

Article

Developing abundant rare-earth iron perovskite electrodes for high-performance and low-cost solid oxide fuel cells

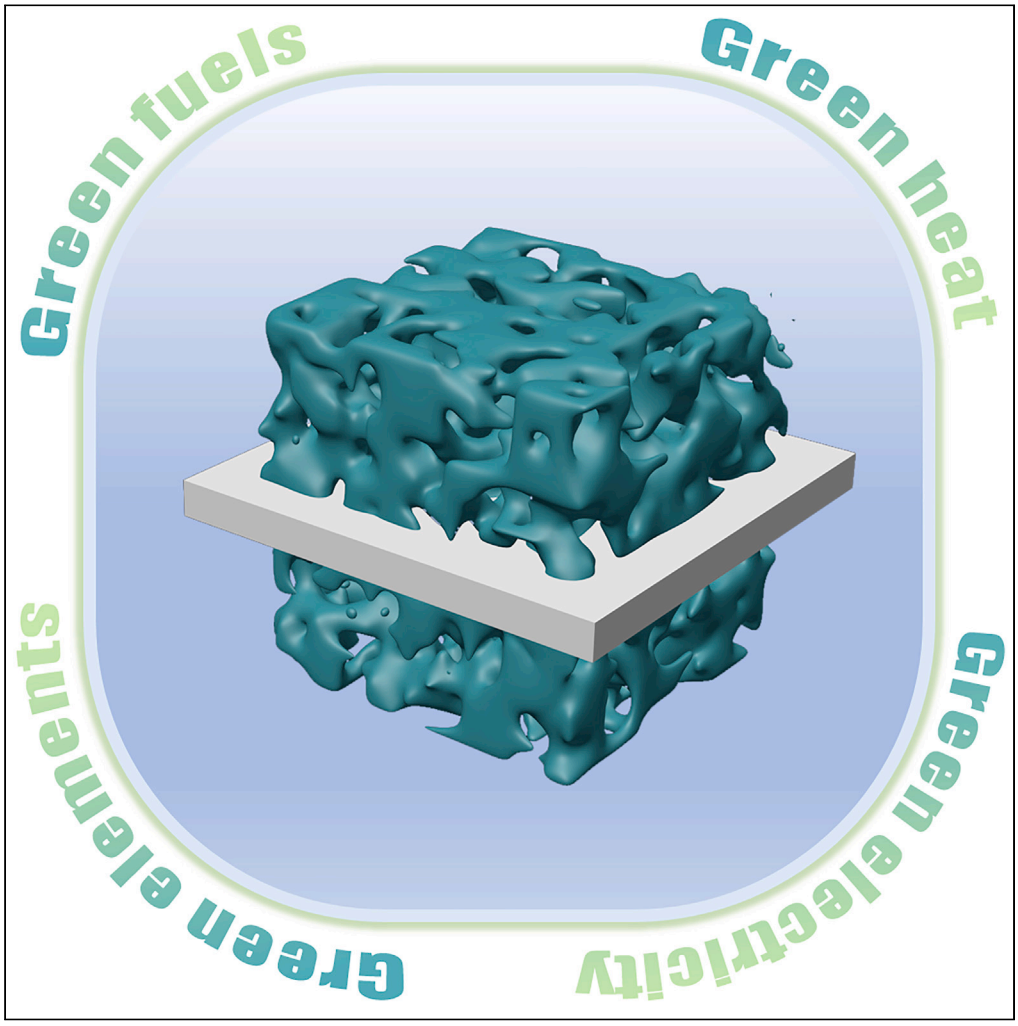

Kai Song, Fang Wang, Jinqiu Zhang, ..., Dong Tian, Yihan Ling, Bin Lin

f-wang-ssi@foxmail.com (F.W.)
lyhyy@cumt.edu.cn (Y.L.)
bin@uestc.edu.cn (B.L.)

Highlights

Abundant rare-earth iron perovskite electrodes are proposed for fuel cells

All three electrodes display a cubic perovskite phase and chemical compatibility

All three electrodes possess exceptional surface oxygen exchange ability

All single cells with rare-earth iron electrodes show high output performance

Song et al., iScience 27, 109982
June 21, 2024
https://doi.org/10.1016/j.isci.2024.109982

iScience

CellPress
OPEN ACCESS

Article

Developing abundant rare-earth iron perovskite electrodes for high-performance and low-cost solid oxide fuel cells

Kai Song,[1,2,3] Fang Wang,[1,2,*] Jinqiu Zhang,[4] Biao Niu,[4] Cheng Cheng Wang,[5] Halefom G. Desta,[6] Xing Gao,[3] Dong Tian,[3] Yihan Ling,[4,*] and Bin Lin[3,6,7,*]

SUMMARY

The swift advancement of the solid oxide fuel cell (SOFC) sector necessitates a harmony between electrode performance and commercialization cost. The economic value of elements is frequently linked to their abundance in the Earth's crust. Here, we develop abundant rare-earth iron perovskite electrodes of $Ln_{0.6}Sr_{0.4}FeO_{3-\delta}$ (Ln = La, Pr, and Nd) with high abundant rare-earth metals and preferred iron metal for SOFCs. All three symmetric electrode materials display a cubic perovskite phase and excellent chemical compatibility with $Gd_{0.2}Ce_{0.8}O_{2-\delta}$ electrolyte. All three electrodes possess exceptional surface oxygen exchange ability. At 800°C, single cells with $La_{0.6}Sr_{0.4}FeO_{3-\delta}$, $Pr_{0.6}Sr_{0.4}FeO_{3-\delta}$, and $Nd_{0.6}Sr_{0.4}FeO_{3-\delta}$ symmetric electrodes attained excellent open circuit voltages of 1.108, 1.101, and 1.097 V, respectively, as well as peak powers of 213.52, 281.12, and 254.58 mW cm^{-2}. The results suggest that overall performance of abundant rare-earth iron perovskite electrodes has a favorable impact on the extensive expansion of SOFCs, presenting significant potential for practical applications.

INTRODUCTION

Since the industrial revolution, the use of energy has become diversified; from the initial direct use of thermal energy to the gradual transition to electricity as the main form of industrialization, the way of energy utilization has gradually changed.[1–3] After the carbon neutrality goal was proposed, people paid more attention to energy efficiency and greenhouse gas emissions, therefore, renewable energy utilization was regarded as a solution to the energy crisis and energy transition.[4,5] In the past few decades, solid oxide fuel cells (SOFCs) have been widely recognized as promising for their high energy conversion efficiency, low emissions, and wide range of fuel adaptability.[6–8] However, their application scenarios are also limited by their high operating temperature and other conditions, which also pose high requirements on the performance of electrodes, electrolytes, and other materials under high temperature conditions.[9–11]

Electrolyte materials as excellent high-temperature oxygen ion conductors have been able to be commercially produced in a mature and stable manner.[12,13] In terms of electrode research, people have gradually shifted from using precious metals such as platinum, palladium, and ruthenium to perovskite-based ceramic functional materials; researchers have doped a large amount of perovskite materials, which are generally based on ABO_3 and doped with a large amount of rare earth elements (La, Pr, Nd, Yb, Sc and Y) on the A site, and the B site is generally composed of transition metal elements (Fe, Co, Ni, Cu, Zn, Mn, Mo, Nb and V).[14–19] But the vigorous development of SOFC industry inevitably accompanies the large-scale use of electrode materials. One factor that cannot be ignored is that the cost of materials is positively correlated with the abundance of their constituent elements in the crust (abundance) and the difficulty of extraction. The cost of materials is closely related to the overall economy of SOFCs.[20,21] Therefore, it is very important to choose a suitable composition of a material for SOFC electrodes with long-term commercial development.[22,23]

As shown in Figure 1, most elements in the crust are arranged intuitively according to their abundance.[24–26] Many scholars have verified that the typical combination of A site in perovskite is rare earth elements doped with Sr elements, which can effectively suppress Sr segregation and improve oxygen reduction-oxidation catalytic activity.[27,28] As shown in Figure 1, except for Ce which is easy to form fluorite structure, it can be seen that La, Pr, and Nd have higher abundance among rare earth elements. Among the B site elements, transition metal elements with multiple valence states are the main components.[29] Iron (Fe), the second most abundant metal element in the crust, has higher

[1]School of Materials Science and Engineering, Changchun University of Science and Technology, No. 7989 Weixing Road, Changchun 130022, China
[2]Zhongshan Institute of Changchun University of Science and Technology, No. 16 Huizhandong Road, Huoju Development District, Zhongshan 528437, China
[3]Anhui Province Key Laboratory of Low-Temperature Co-Fired Materials, Huainan Normal University, Huainan 232038, China
[4]School of Materials Science and Physics, China University of Mining and Technology, Xuzhou 221116, China
[5]Shen Zhen Polytechnic University, Shenzhen 518055, China
[6]School of Mechanical and Electrical Engineering, University of Electronic Science and Technology of China, Chengdu 611731, China
[7]Lead contact
*Correspondence: f-wang-ssi@foxmail.com (F.W.), lyhyy@cumt.edu.cn (Y.L.), bin@uestc.edu.cn (B.L.)
https://doi.org/10.1016/j.isci.2024.109982

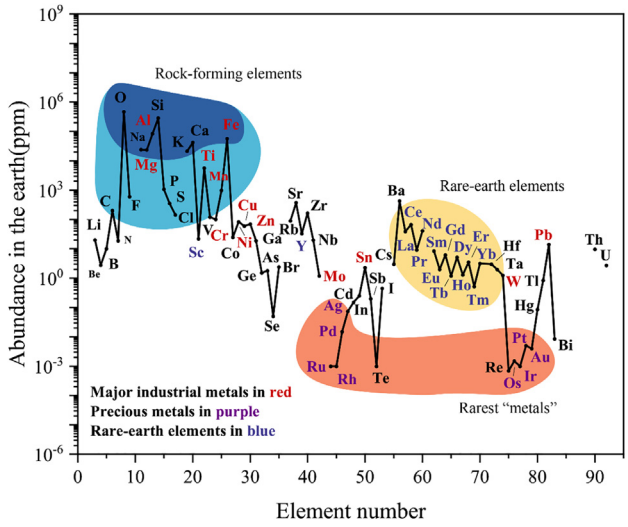

Figure 1. Abundance of elements in the earth's crust

catalytic activity and extremely stable raw material supply than Co, Mn, and other elements due to its multiple oxidation states.[30] The aforementioned advantages indicate that $SrFeO_{3-\delta}$ based functional ceramic electrodes are promising electrode materials for future development.[27,28,31,32] Based on this, we explore A site La, Pr, and Nd three kinds of rare earth doping, and apply them to symmetrical solid oxide fuel cells with simple structure and easy to prepare on a large scale for verification. We comprehensively compare their phase composition, micro-lattice structure, thermo-mechanical, and electrochemical properties under reducing conditions from a horizontal perspective. We aim to find out the most sustainable fuel cell electrode materials.

RESULTS AND DISCUSSION

As shown in Figure 2A, XRD patterns of the synthesized $La_{0.6}Sr_{0.4}FeO_{3-\delta}$, $Pr_{0.6}Sr_{0.4}FeO_{3-\delta}$ and $Nd_{0.6}Sr_{0.4}FeO_{3-\delta}$ show that the LSF, PSF, and NSF are fully doped into the $SrFeO_{3-\delta}$ lattice, with no impurity peaks, indicating that the synthesized materials are pure phase. As shown in Figure 2B, to analyze the effect of La, Pr and Nd doping on the lattice size in detail, the enlarged results of 2θ range from 31°–34° show that the diffraction peaks of the three materials move to higher angles successively; as shown in Table 1, this is due to the change of atomic radius of the three elements, which causes lattice distortion and leads to angular shift of diffraction peaks.

$Y_{0.16}Zr_{0.84}O_{1.92}$ (YSZ), as a successful and excellent oxygen ion conductor, is widely used as the electrolyte for solid oxide fuel cells. However, under high temperature conditions, the Sr element commonly used in the electrode materials tends to react with the Zr element in YSZ, forming $SrZrO_3$, which is unfavorable for the electrode catalytic reaction, as shown in Figure 1C. Therefore, it is common to spin-coat a GDC transition layer between the YSZ electrolyte and the electrode to prevent the contact of the two parts while ensuring the oxygen ion conductivity, as shown in Figure 2D.

To further evaluate the microstructural characteristics of LSF, PSF and NSF, transmission electron microscopy (TEM) and high-resolution TEM (HR-TEM) techniques were used to detect their atomic-scale arrangement. As shown in Figures 3A–3C, the macroscopic morphology of LSF, PSF and NSF are porous materials, with many defects and facets. All three materials show obvious lattice fringes after doping, indicating excellent crystallinity. As shown in Figures 3D–3F, Fast Fourier transform (FFT) analysis of LSF, PSF, and NSF revealed diffraction fringes with lattice spacing of 0.372 nm, 0.399 nm, and 0.404 nm for the (012) plane, respectively. The ordered change of lattice spacing is related to the change of atomic radius of the A-site doping elements. As shown in Figure S1, the thermal expansion coefficients of LSF, PSF, and NSF are $16.9 \times 10^{-6}\ K^{-1}$, $16.7 \times 10^{-6}\ K^{-1}$, and $16.7 \times 10^{-6}\ K^{-1}$, respectively, which can perform a good thermal match with electrolytes.

The XPS results of LSF, PSF and NSF are shown in Figure 4. Since Fe generally exists in three different oxidation states in the compounds, Fe^{2+} and Fe^{4+} have higher catalytic activity than Fe^{3+} due to the unstable valence state formed by the external charge. To evaluate the effect of A-site La, Pr and Nd substitution on the oxidation state of B-site Fe, the Fe 2p measurements are shown in Figures 4A–4C, respectively. The typical Fe 2p3/2 and Fe 2p1/2 peaks can be observed in the spectrum. As shown by the fitted Fe 2p spectra, the peaks at 709.43 eV and 722.58 eV in Figure 4A correspond to Fe 2p2/3 and Fe 2p1/2 of Fe^{2+}, respectively, the peaks at 710.38 eV and 723.93 eV correspond to Fe 2p2/3 and Fe 2p1/2 of Fe^{3+}, respectively, the peaks at 713.73 eV and 727.13 eV correspond to Fe 2p2/3 and Fe 2p1/2 of Fe^{4+}, respectively, and the peaks at 718.23 eV and 731.88 eV are satellite peaks of X-ray photoelectron spectroscopy (XPS). The XPS images of Sr in the supplemental information Figure S2. The comparison of the relative content of different valence states of Fe elements in LSF, PSF, and NSF is shown in Figure 4G, where it can be observed that the proportion of Fe^{2+} and Fe^{4+} ions with higher catalytic activity has increased significantly in PSF. In addition to the Fe 2p spectra, the fitted O1s spectra are shown in Figures 4D–4F, where the peak at 529 eV is attributed to lattice

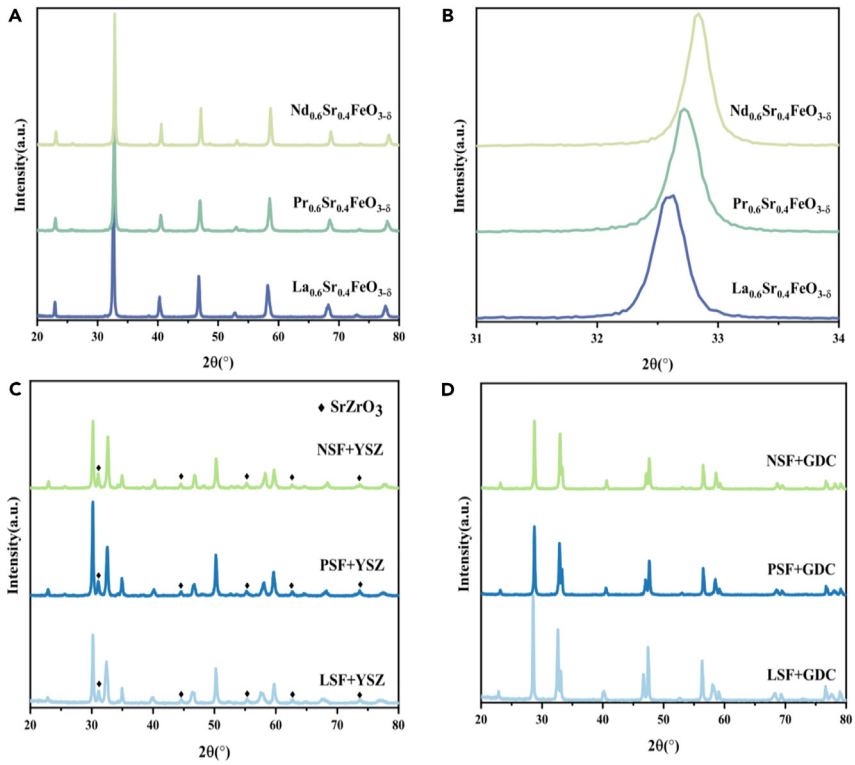

Figure 2. XRD patterns of LSF, PSF and NSF (A and B); Chemical compatibility of LSF, PSF and NSF with electrolyte materials YSZ and GDC (C and D)

oxygen, and the peak at 531 eV is carbonate species (CO_3^{2-}), further confirming the formation of $SrCO_3$ and adsorbed oxygen. The adsorbed oxygen is mainly composed of O^{2-}, O_2^{2-}, O^-, etc., and the oxygen conversion process can be described as follows:

$$O_2 \leftrightarrow O_2 \xrightarrow{+e^-} O_2^- \xrightarrow{+e^-} O_2^{2-} \leftrightarrow 2O^- \xrightarrow{+2e^-} 2O^{2-}$$

The relative ratio of lattice oxygen and adsorbed oxygen in LSF, PSF, and NSF is similar, as shown in Figure 4G, indicating that the doping of three A-site elements has no effect on the ratio of lattice oxygen and adsorbed oxygen. The improvement of catalytic activity may be related to the change of ratio between Fe^{3+} and Fe^{4+}.

The electrochemical activity of LSF, PSF and NSF for oxygen reduction and fuel oxidation was evaluated by analyzing the electrochemical impedance spectra (EIS). Symmetric cells with LnSF/GDC/YSZ/GDC/LnSF (Ln = La, Pr and Nd) structure were fabricated to test the impedance. The electrochemical impedance of LSF, PSF, and NSF electrodes measured in air and hydrogen is shown in Figure 5 as typical Nyquist plots. Usually, the intercept of the EIS spectrum in the high frequency range corresponds to the ohmic resistance, and the difference between the intercept of the spectrum and the axis in the whole range is the polarization resistance. There is a positive correlation between the change of electrical conductivity and the change of ohmic impedance of the material, and the electrical conductivity data under air atmosphere are shown in Figure S3. By doping A-site La, Pr and Nd, the air atmosphere polarization resistances at 800°C were 0.35 Ω cm^2, 0.27 Ω cm^2 and 0.48 Ω cm^2, respectively, and the hydrogen atmosphere polarization resistances were 0.56 Ω cm^2, 0.26 Ω cm^2 and 0.98 Ω cm^2, the impedance variation rules of the three materials can be learned from Figure S4. As shown in the Table S1, compared with several commercialized electrode materials such as LSCF etc. in terms of comprehensive electrochemical performance and crust element abundance, LSF, PSF and NSF showed higher or more competitive performance.

To analyze the electrochemical reaction process in the impedance test in detail, the distribution of relaxation time (DRT) was introduced. As shown in Figures 6A and 6B, the spectra of LSF, PSF, and NSF measured at 800°C under different atmospheres can be roughly separated

Table 1. Ionic radii of common rare earth elements

Ion	La^{3+}	Ce^{3+}	Pr^{3+}	Nd^{3+}	Sm^{3+}	Gd^{3+}
Atomic number	57	58	59	60	62	64
Ionic radius(pm)	103.2	102	99	98.3	95.8	93.8
Coordination number	8/12	8/12	8/12	8/12	8/12	8/12

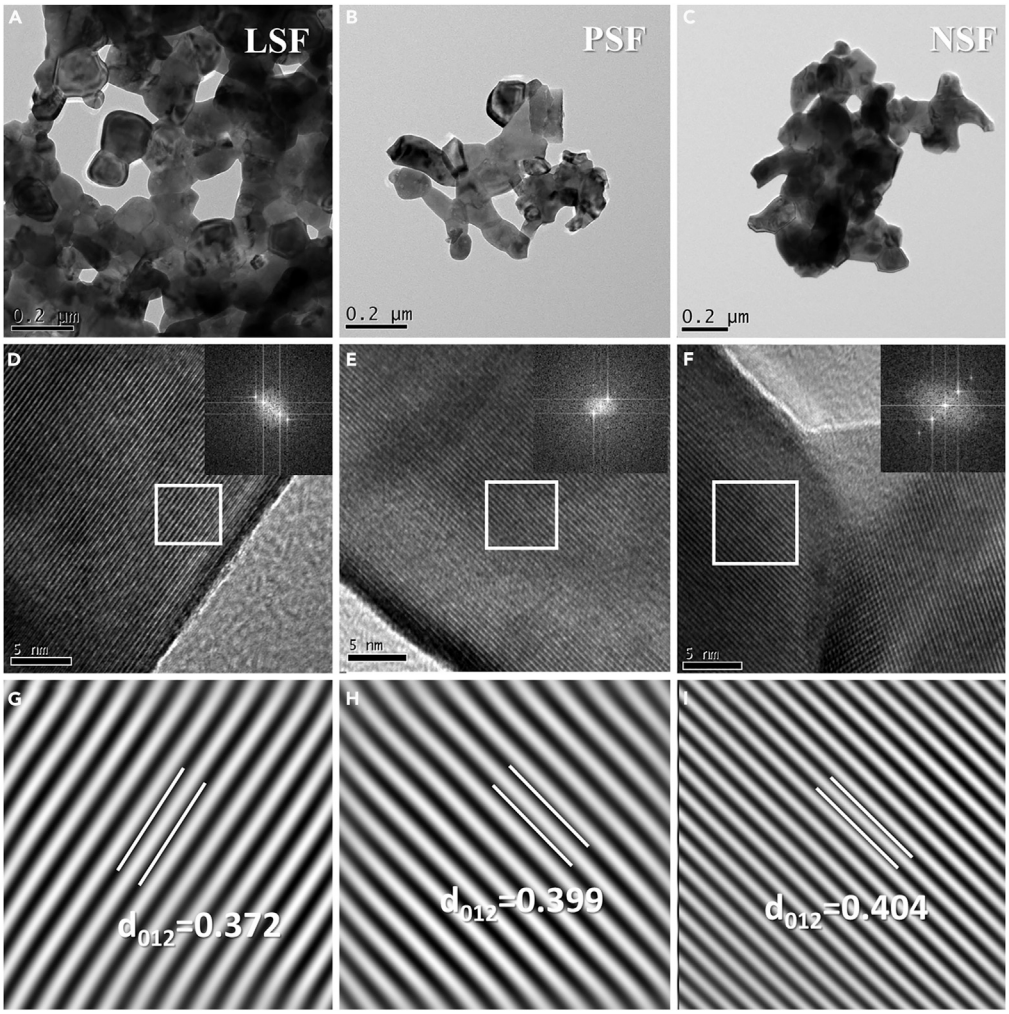

Figure 3. Transmission electron microscopy images; the micro-grain images of LSF, PSF and NSF correspond to (A–C); the fast Fourier transform images correspond to (D–F); the micro-lattice spacing correspond to (G–I)

into several peaks, P1, P2, P3, P4 and P5, and the peak area is positively correlated with the resistance value. P1 is related to gas adsorption, dissociation, and surface diffusion process. P2 is related to bulk diffusion to the triple phase boundary process. P3, P4 and P5 are attributed to hydrogen/oxygen incorporation and charge transfer process. The resistance of P1-P5 can be calculated by analyzing the peak area. Clearly, P1 and P2 form a certain gradient among LSF, PSF and NSF materials, where PSF has a smaller resistance value than the other two materials. Therefore, the performance improvement is attributed to Pr doping, which enhances the surface diffusion and bulk diffusion efficiency.

Single cells with LnSF|GDC|ScZ|GDC|LnSF (Ln = La, Pr and Nd) configuration were prepared and tested for electrochemical performance using H_2 as fuel in the temperature range of 800°C–650°C. As shown in Figure 7, the measured open circuit voltage (OCV) values of LSF, PSF, and NSF symmetric cells at 800°C were 1.108 V, 1.10 V and 1.097 V, respectively, indicating that a dense electrolyte support and a good cell sealing technique were obtained during the cell fabrication process. As shown in Figures 7A–7C, the measured current density-voltage curves showed linear behavior, indicating that both the anode and cathode had sufficient gas transport characteristics. The maximum power densities (MPD) of LSF, PSF, and NSF symmetric cells measured at 800°C were 213.5, 281.1 and 254.6 mW cm^{-2}. As shown in Figure 7G, PSF had the highest power density among the three, which was consistent with the EIS and DRT analysis results. The MPD of PSF were 281.1, 151.0, 85.4 and 43.0 mW cm^{-2}. The performance improvement was attributed to Pr substitution, which increased the lattice distortion and opened pathways for oxygen ion migration, and expanded the reaction area for oxygen reduction and fuel oxidation reactions, thus improving the electrochemical performance.

The EIS of LSF, PSF and NSF symmetric cells are shown in Figures 7D–7F. The cell polarization resistance of LSF, PSF and NSF are shown in the Figure S5, which were 0.98, 0.85 and 0.94 Ω at 800°C, respectively. The same ohmic resistance values indicate that the performance is determined by the polarization resistance. As shown in Figure 7G, the comparison of R_p by comparing La, Pr, and Nd three A-site doping elements, the polarization resistances at 800°C were 0.48, 0.27 and 0.35 Ω, respectively. As shown in Figure 7H, DRT data were derived by

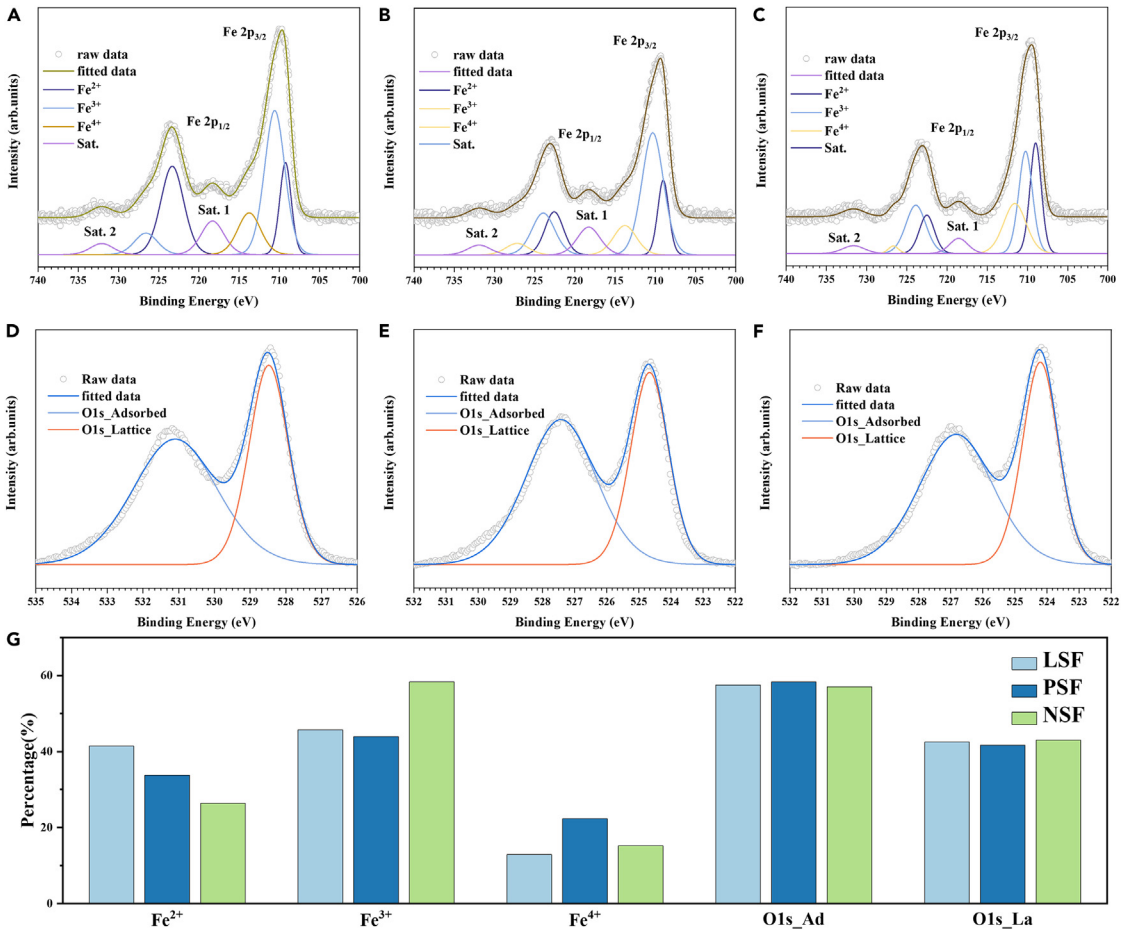

Figure 4. Fe element XPS images of LSF, PSF and NSF are (A–C), respectively; O element XPS images are (D–F), respectively; comparison of relative contents of Fe element and O element (G)

using EIS data for calculation, which showed that in the overall cell performance, P1 and P2 processes of PSF had relatively small resistance values, indicating that gas could smoothly undergo adsorption, dissociation, and diffusion processes on the electrode surface, which also confirmed the previous electrochemical analysis of electrode materials under different atmospheres. In addition, as shown in Figure 7I, PSF|GDC|YSZ|GDC|PSF cell was tested for long-term performance, reaching 90 h without any signs of degradation. As shown in Figure 8, scanning electron microscopy was used to observe the microscopic morphology of the cell after long-term stable operation for 90 h.

Conclusion

This paper screened the elements of perovskite-type fuel cell electrodes suitable for large-scale applications and selected three rare earth elements La, Pr and Nd with the highest abundance in the crust and Fe, the most abundant transition element, to characterize their performance. We successfully prepared LSF, PSF and NSF three electrode materials and studied their electrochemical performance in different environments in detail. XPS showed that the different doping of the three materials directly affected the formation of various oxidation states of Fe, which improved the catalytic activity. Through EIS test and DRT analysis, the three materials showed good electrochemical performance. At 800°C, the symmetric single cells with LSF, PSF and NSF as electrodes achieved good open circuit voltages (OCVs) of 1.108 V, 1.101 V and 1.097 V, respectively, and peak power of 213.5 mW cm^{-2}, 281.1 mW cm^{-2} and 254.6 mW cm^{-2}, respectively. The comprehensive performance of three electrode materials has positive significance for large-scale development of solid oxide fuel cells, among which PSF as the most excellent electrode material in terms of electrochemical performance has broad application prospects and practicality.

Limitations of the study

This work has studied how to maintain a balance between the performance and cost of solid oxide fuel cells in terms of electrodes. However, electrolyte materials still account for a significant portion of the costs. Future work will focus on a systematic study of the overall performance and cost of the fuel cell stack.

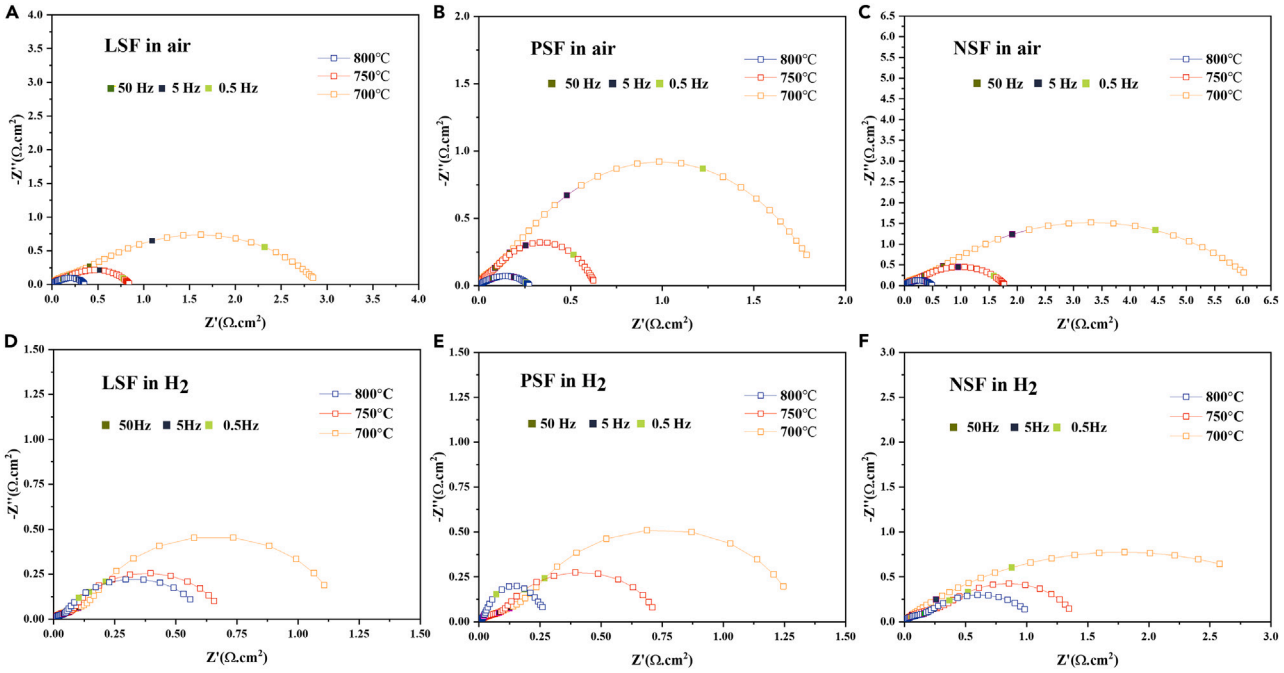

Figure 5. Typical electrochemical impedance spectra of LSF, PSF and NSF in air atmosphere (A–C) and hydrogen atmosphere (D–F), respectively

STAR★METHODS

Detailed methods are provided in the online version of this paper and include the following:

- KEY RESOURCES TABLE
- RESOURCE AVAILABILITY
  - Lead contact
  - Materials availability
  - Data and code availability
- EXPERIMENTAL MODEL AND STUDY PARTICIPANT DETAILS
- METHOD DETAILS
  - Materials synthesis and cell fabrication
  - Material characterization

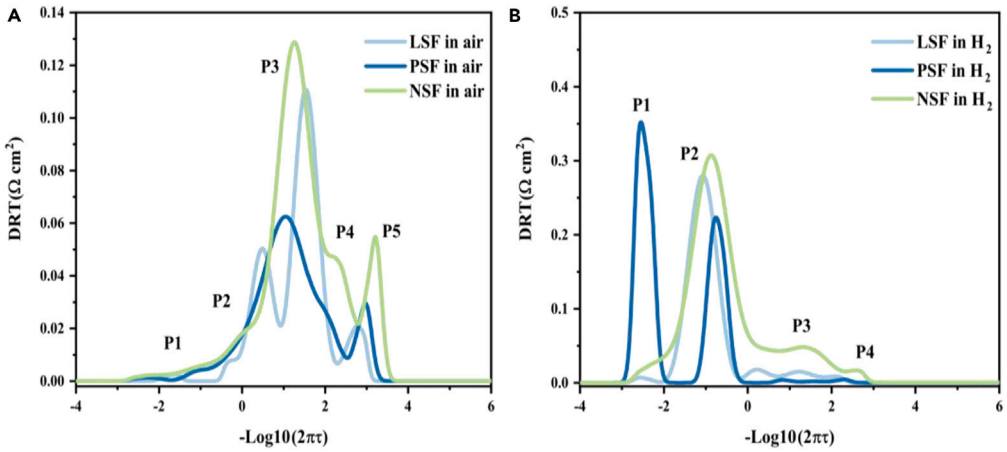

Figure 6. DRT image derived from calculation of EIS data measured by LSF, PSF and NSF at 800°C: in air atmosphere (A) and hydrogen atmosphere (B)

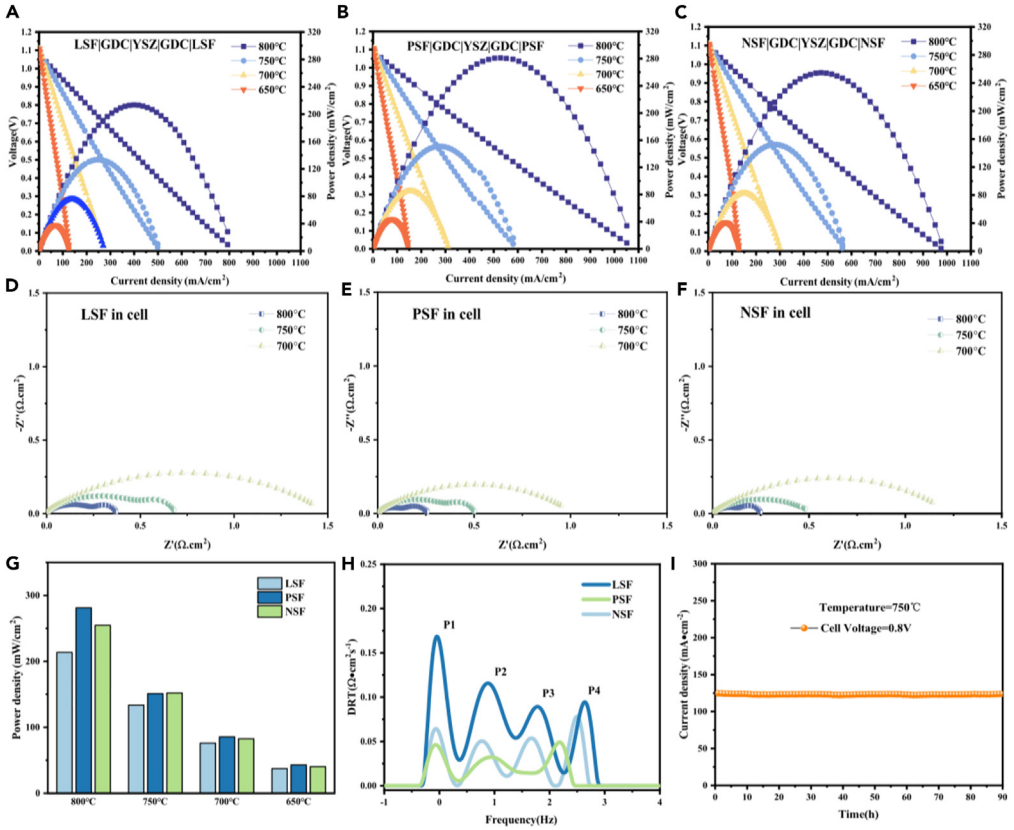

Figure 7. I-V curves of symmetrical cells with (A) LSF, (B) PSF, and (C) NSF as fuel electrodes (A–C); typical electrochemical impedance spectra of single cells measured at OCV condition (D–F); Power comparison of three cell at different temperatures (G); cell DRT images derived from EIS (H); long-term performance of cell with PSF as electrode material (I)

- QUANTIFICATION AND STATISTICAL ANALYSIS
- ADDITIONAL RESOURCES

SUPPLEMENTAL INFORMATION

Supplemental information can be found online at https://doi.org/10.1016/j.isci.2024.109982.

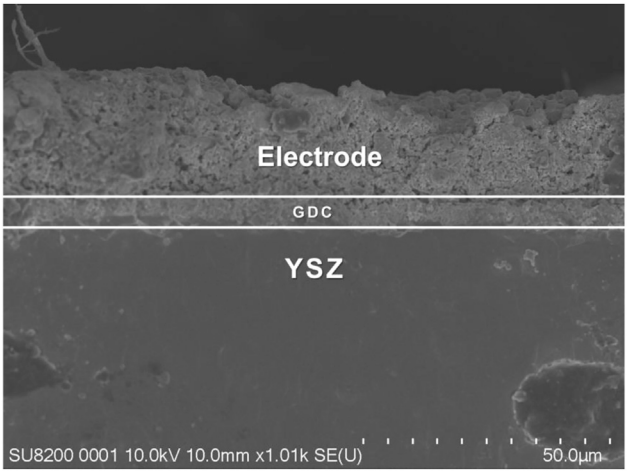

Figure 8. Microstructure of the cell after long-term stable operation for 90 h

ACKNOWLEDGMENTS

This work is funded by International Cooperation Foundation (20220402026GH) of Science and Technology Department of Jilin Province and innovative research team project (CXTD2023009) introduced by Zhongshan Institute of Changchun University of Science and Technology, the Key Project of Scientific Research Foundation of Anhui Province Education Department (KJ2021A0961), the 2022 Shenzhen Science and Technology Program (GJHZ20210705142006020), and the Science and Technology Department of Sichuan Province (2023YFG0202).

AUTHOR CONTRIBUTIONS

K.S.: methodology, investigation, and writing – original draft. F.W.: methodology, investigation, and supervision. J.Z.: methodology and writing – review and editing. B.N.: methodology and writing – review and editing. C.C.W.: Writing – review and editing. H.G.D.: Writing – review and editing. X.G.: data curation. D.T.: data curation and Supervision. Y.L.: formal analysis, funding acquisition, and supervision. B.L.: conceptualization, supervision, and writing – review and editing.

DECLARATION OF INTERESTS

The authors declare no competing interests.

Received: November 27, 2023
Revised: March 10, 2024
Accepted: May 13, 2024
Published: May 15, 2024

REFERENCES

1. Zhang, Y., Chen, B., Guan, D., Xu, M., Ran, R., Ni, M., Zhou, W., O'Hayre, R., and Shao, Z. (2021). Thermal-expansion offset for high-performance fuel cell cathodes. Nature *591*, 246–251. https://doi.org/10.1038/s41586-021-03264-1.
2. Liu, F., Deng, H., Diercks, D., Kumar, P., Jabbar, M.H.A., Gumeci, C., Furuya, Y., Dale, N., Oku, T., Usuda, M., et al. (2023). Lowering the operating temperature of protonic ceramic electrochemical cells to <450 °C. Nat. Energy *8*, 1145–1157. https://doi.org/10.1038/s41560-023-01350-4.
3. Punia, A., Singh, R.P., and Chauhan, N.S. (2023). Drivers of Climate Migration. Global Climate Change and Environmental Refugees (Springer), pp. 57–75. https://doi.org/10.1007/978-3-031-24833-7_4.
4. Lu, N., Zhang, Z., Wang, Y., Li, H.B., Qiao, S., Zhao, B., He, Q., Lu, S., Li, C., Wu, Y., et al. (2022). Enhanced low-temperature proton conductivity in hydrogen-intercalated brownmillerite oxide. Nat. Energy *7*, 1208–1216. https://doi.org/10.1038/s41560-022-01166-8.
5. Yang, Y., Chen, Z., Li, M., Rao, M., Jin, F., Ling, Y., Feng, P., and Wang, S. (2023). A highly efficient bismuth substitution induced A-site ordered layered perovskite electrode for symmetrical solid oxide fuel cells. J. Mater. Chem. A Mater. *11*, 7995–8002. https://doi.org/10.1039/d2ta08892d.
6. Duan, C., Kee, R., Zhu, H., Sullivan, N., Zhu, L., Bian, L., Jennings, D., and O'Hayre, R. (2019). Highly efficient reversible protonic ceramic electrochemical cells for power generation and fuel production. Nat. Energy *4*, 230–240. https://doi.org/10.1038/s41560-019-0333-2.
7. Song, Y., Zhang, X., Xie, K., Wang, G., and Bao, X. (2019). High-Temperature CO_2 Electrolysis in Solid Oxide Electrolysis Cells: Developments, Challenges, and Prospects. Adv. Mater. *31*, 1902033. https://doi.org/10.1002/adma.201902033.
8. Boldrin, P., and Brandon, N.P. (2019). Progress and outlook for solid oxide fuel cells for transportation applications. Nat. Catal. *2*, 571–577. https://doi.org/10.1038/s41929-019-0310-y.
9. Mushtaq, N., Lu, Y., Xia, C., Dong, W., Wang, B., Shah, M.Y., Rauf, S., Akbar, M., Hu, E., Raza, R., et al. (2021). Promoted electrocatalytic activity and ionic transport simultaneously in dual functional $Ba_{0.5}Sr_{0.5}Fe_{0.8}Sb_{0.2}O_{3-\delta}$-$Sm_{0.2}Ce_{0.8}O_{2-\delta}$ heterostructure. Appl. Catal. B Environ. *298*, 120503. https://doi.org/10.1016/j.apcatb.2021.120503.
10. Wang, X., Wei, K., Yan, S., Wu, Y., Kang, J., Feng, P., Wang, S., Zhou, F., and Ling, Y. (2020). Efficient and stable conversion of oxygen-bearing low-concentration coal mine methane by the electrochemical catalysis of SOFC anode: From pollutant to clean energy. Appl. Catal. B Environ. *268*, 118413. https://doi.org/10.1016/j.apcatb.2019.118413.
11. Niu, B., Lu, C., Yi, W., Luo, S., Li, X., Zhong, X., Zhao, X., and Xu, B. (2020). In-situ growth of nanoparticles-decorated double perovskite electrode materials for symmetrical solid oxide cells. Appl. Catal. B Environ. *270*, 118842. https://doi.org/10.1016/j.apcatb.2020.118842.
12. Fan, L. (2020). Solid-state electrolytes for SOFC. Solid Oxide Fuel Cells: From Electrolyte-Based to Electrolyte-Free Devices (Wiley), pp. 35–78. https://doi.org/10.1002/9783527812790.ch2.
13. Kaur, G. (2019). Intermediate Temperature Solid Oxide Fuel Cells: Electrolytes, Electrodes and Interconnects, pp. 12–15. https://doi.org/10.1016/C2018-0-00575-7.
14. Wan, Z., Tao, Y., Shao, J., Zhang, Y., and You, H. (2021). Ammonia as an effective hydrogen carrier and a clean fuel for solid oxide fuel cells. Energy Convers. Manag. *228*, 113729. https://doi.org/10.1016/j.enconman.2020.113729.
15. Jiang, S.P. (2019). Development of lanthanum strontium cobalt ferrite perovskite electrodes of solid oxide fuel cells – A review. Int. J. Hydrogen Energy *44*, 7448–7493. https://doi.org/10.1016/j.ijhydene.2019.01.212.
16. Lv, H., Lin, L., Zhang, X., Gao, D., Song, Y., Zhou, Y., Liu, Q., Wang, G., and Bao, X. (2019). In situ exsolved $FeNi_3$ nanoparticles on nickel doped $Sr_2Fe_{1.5}Mo_{0.5}O_{6-\delta}$ perovskite for efficient electrochemical CO_2 reduction reaction. J. Mater. Chem. A Mater. *7*, 11967–11975. https://doi.org/10.1039/c9ta03065d.
17. Sun, C., Alonso, J.A., and Bian, J. (2021). Recent Advances in Perovskite-Type Oxides for Energy Conversion and Storage Applications. Adv. Energy Mater. *11*, 2000459. https://doi.org/10.1002/aenm.202000459.
18. Küngas, R. (2020). Review - Electrochemical CO_2 Reduction for CO Production: Comparison of Low- And High-Temperature Electrolysis Technologies. J. Electrochem. Soc. *167*, 044508. https://doi.org/10.1149/1945-7111/ab7099.
19. Singh, M., Zappa, D., and Comini, E. (2021). Solid oxide fuel cell: Decade of progress, future perspectives and challenges. Int. J. Hydrogen Energy *46*, 27643–27674. https://doi.org/10.1016/j.ijhydene.2021.06.020.
20. Valente, A., Iribarren, D., and Dufour, J. (2019). End of life of fuel cells and hydrogen products: From technologies to strategies. Int. J. Hydrogen Energy *44*, 20965–20977. https://doi.org/10.1016/j.ijhydene.2019.01.110.
21. Al-Khori, K., Bicer, Y., and Koç, M. (2020). Integration of Solid Oxide Fuel Cells into oil and gas operations: needs, opportunities, and challenges. J. Clean. Prod. *245*, 118924. https://doi.org/10.1016/j.jclepro.2019.118924.
22. Song, Y., Chen, Y., Wang, W., Zhou, C., Zhong, Y., Yang, G., Zhou, W., Liu, M., and Shao, Z. (2019). Self-Assembled Triple-Conducting Nanocomposite as a Superior Protonic Ceramic Fuel Cell Cathode. Joule *3*, 2842–2853. https://doi.org/10.1016/j.joule.2019.07.004.
23. Emadi, M.A., Chitgar, N., Oyewunmi, O.A., and Markides, C.N. (2020). Working-fluid selection and thermoeconomic optimisation of a combined cycle cogeneration dual-loop organic Rankine cycle (ORC) system for solid oxide fuel cell (SOFC) waste-heat recovery.

Appl. Energy *261*, 114384. https://doi.org/10.1016/j.apenergy.2019.114384.

24. Weng, Z., Jowitt, S.M., Mudd, G.M., and Haque, N. (2015). A detailed assessment of global rare earth element resources: Opportunities and challenges. Econ. Geol. *110*, 1925–1952. https://doi.org/10.2113/econgeo.110.8.1925.
25. Batapola, N.M., Dushyantha, N.P., Premasiri, H.M.R., Abeysinghe, A.M.K.B., Rohitha, L.P.S., Ratnayake, N.P., Dissanayake, D.M.D.O.K., Ilankoon, I.M.S.K., and Dharmaratne, P.G.R. (2020). A comparison of global rare earth element (REE) resources and their mineralogy with REE prospects in Sri Lanka. J. Asian Earth Sci. *200*, 104475. https://doi.org/10.1016/j.jseaes.2020.104475.
26. Dushyantha, N., Batapola, N., Ilankoon, I.M.S.K., Rohitha, S., Premasiri, R., Abeysinghe, B., Ratnayake, N., and Dissanayake, K. (2020). The story of rare earth elements (REEs): Occurrences, global distribution, genesis, geology, mineralogy and global production. Ore Geol. Rev. *122*, 103521. https://doi.org/10.1016/j.oregeorev.2020.103521.
27. Hou, Y., Wang, L., Bian, L., Zhang, Q., Chen, L., and Chou, K.C. (2022). Effect of high-valence elements doping at B site of $La_{0.5}Sr_{0.5}FeO_{3-\delta}$. Ceram. Int. *48*, 4223–4229. https://doi.org/10.1016/j.ceramint.2021.10.214.
28. Kumar, S., Das, A., and Omar, S. (2023). Electrochemical Performance of $SrFeO_{3-\delta}$ for Application as a Symmetric Electrode in Solid Oxide Fuel Cells. ACS Appl. Energy Mater. *6*, 2049–2062. https://doi.org/10.1021/acsaem.2c04034.
29. Zou, Z., Li, Y., Lu, Z., Wang, D., Cui, Y., Guo, B., Li, Y., Liang, X., Feng, J., Li, H., et al. (2020). Mobile Ions in Composite Solids. Chem. Rev. *120*, 4169–4221. https://doi.org/10.1021/acs.chemrev.9b00760.
30. Dey, S., Das, S., Chaudhary, S., Parvatalu, D., Mukhopadhyay, M., Paul, S., Das Sharma, A., and Mukhopadhyay, J. (2023). Advancing insights towards electrocatalytic activity of La/Ba-Sr-Co-Fe-O-based perovskites for oxygen reduction & evolution process in reversible solid oxide cell. Scripta Mater. *229*, 115380. https://doi.org/10.1016/j.scriptamat.2023.115380.
31. Su, T., Zhang, T., Xie, H., Zhong, J., and Xia, C. (2022). Investigation into structure and property of W and Ti co-doped $SrFeO_3$ perovskite as electrode of symmetrical solid oxide fuel cell. Int. J. Hydrogen Energy *47*, 16272–16282. https://doi.org/10.1016/j.ijhydene.2022.03.130.
32. Batuk, M., Vandemeulebroucke, D., Ceretti, M., Paulus, W., and Hadermann, J. (2023). Topotactic redox cycling in $SrFeO_{2.5+\delta}$ explored by 3D electron diffraction in different gas atmospheres. J. Mater. Chem. A Mater. *11*, 213–220. https://doi.org/10.1039/d2ta03247c.
33. Yang, Y., Wu, Y., Bao, H., Song, W., Ni, H., Tian, D., Lin, B., Feng, P., and Ling, Y. (2020). An efficient and prospective self-assembled hybrid electrocatalyst for symmetrical and reversible solid oxide cells. Electrochim. Acta *362*, 137171. https://doi.org/10.1016/j.electacta.2020.137171.
34. Song, K., Yu, Z., Luo, X., Zhu, S., Yang, Y., Yang, Q., Tian, D., Lu, X., Ding, Y., Chen, Y., and Lin, B. (2020). A simple Ce-doping strategy to enhance stability of hybrid symmetrical electrode for solid oxide fuel cells. Int. J. Hydrogen Energy *45*, 29259–29270. https://doi.org/10.1016/j.ijhydene.2020.07.173.

STAR★METHODS

KEY RESOURCES TABLE

REAGENT or RESOURCE	SOURCE	IDENTIFIER
Iron(III) nitrate nonahydrate	Sinopharm Chemical Reagent Co. Ltd.	80072718; CAS: 7782-61-8
Lanthanum(III) nitrate hydrate	Sinopharm Chemical Reagent Co. Ltd.	80073114; CAS: 15878-77-0
Terpineol mixture of isomers	Sinopharm Chemical Reagent Co. Ltd.	30173728; CAS: 8000-41-7

RESOURCE AVAILABILITY

Lead contact

Further information and requests for resources are accessible from the lead contact, Bin Lin (Email: bin@uestc.edu.cn).

Materials availability

This study did not generate new unique reagents. The relevant experimental materials described in this paper and any materials prepared in this paper are available.

Data and code availability

All data reported in this paper will be shared by the lead contact upon request.
This paper does not report original code.
Any additional information required to reanalyze the data reported in this paper is available from the lead contact upon request.

EXPERIMENTAL MODEL AND STUDY PARTICIPANT DETAILS

Not relevant to this study.

METHOD DETAILS

Materials synthesis and cell fabrication

$La_{0.6}Sr_{0.4}FeO_{3-\delta}$ (LSF), $Pr_{0.6}Sr_{0.4}FeO_{3-\delta}$ (PSF) and $Nd_{0.6}Sr_{0.4}FeO_{3-\delta}$ (NSF) powders were synthesized by citric acid-ethylenediaminetetraacetic acid (EDTA) combustion method.[33,34] Taking LSF material as an example, the calculated relative element amounts of $La(NO_3)_3$, $Sr(NO_3)_2$, $Fe(NO_3)_3{\cdot}9H_2O$ were added in deionized water containing a small amount of nitric acid in turn. The molar ratio of citric acid: total metal ions: EDTA was controlled at 1:1:1.5. The pH of the solution was adjusted to 7-8 with the addition of ammonia and the complexation reaction was carried out at 80°C for 3 h, followed by continuous heating until combustion The obtained powder was placed calcined at 1000°C for 3 h. PSF and NSF were prepared by the same method. Use terpineol with a content of 5 wt.% ethyl cellulose, and ball mill with GDC powder sufficiently; then use a spin coater to spin coat the GDC slurry on the YSZ electrolyte sheet at a speed of 5000 r/min, and sinter at 1350°C for 10 h after spin coating twice on each side. $Y_{0.16}Zr_{0.84}O_{1.92}$ (YSZ) and $Gd_{0.2}Ce_{0.8}O_{2-\delta}$ (GDC) powders were both commercial powders purchased from SOFCMAN.

Material characterization

X-ray diffraction (XRD, DX-2800) to study the crystal structure and the chemical compatibility of electrolyte and electrode materials, and to observe whether the dopant elements entered the lattice and whether any unfavorable phase transitions occurred between the electrode and the electrolyte that could affect the stability of the cell. We scanned the sample at a stepwise speed of 20°-80° in air at room temperature using radiation (λ = 0.15418 nm) generated by Cu-Kα on 40 kV and 30 mA of electric current. We performed X-ray photoelectron spectroscopy (XPS, ESCALAB 250Xi, Thermo, US) on powder electrode materials using a single-color Al-Kα radiation (1486.6 eV) as a reference, and calibrated the sample composition and oxidation state using the carbon 1s peak (284.8 eV). We performed high-resolution microstructure analysis on the sample using transmission electron microscope (TEM, TALOS, F200X). We measured the impedance spectra of symmetric cells on an IM6 electrochemical workstation (Zahner, Germany) at a frequency range of 1 MHz–50 mHz and a signal amplitude of 5 mV. We further fitted the impedance spectra with ZSimpWin software. Then we measured the cross section of each unit cell's electrode on an IM6

electrochemical workstation (Zahner, Germany) using air as oxidant and moist hydrogen gas with 3% water as fuel. We obtained I-V curves and I-t curves of long-term output. Finally, we analyzed the cross section of single cells using scanning electron microscope (SEM).

QUANTIFICATION AND STATISTICAL ANALYSIS

Our study doesn't include quantification or statistical analysis.

ADDITIONAL RESOURCES

Our study has not generated or contributed to a new website/forum or not been part of a clinical trial.